

Multi-environment robotic locomotion through integrated pectoral and caudal fin propulsion

Jingshu Peng^{a,1}, Yuanhao Xie^b, Qifan Yang^b, Yongxia Jia^{b,c,*}, Weixi Huang^{b,*}, Guangming Xie^{d,*}

^a*Xingjian College, Tsinghua University, Beijing, 100084, China*

^b*Department of Engineering Mechanics, Tsinghua University, Beijing, 100084, China*

^c*National Experimental Teaching Demonstration Center for Mechanics, Tsinghua University, Beijing, 100084, China*

^d*Intelligent Biomimetic Design Lab, College of engineering, Peking University, Beijing, 100871, China*

Abstract

Amphibious robots, inspired by aquatic and terrestrial animals, play a vital role in advancing robotic capabilities across diverse environments. This study proposes a novel design for stingray-inspired amphibious robots to enhance propulsion efficiency. First, a pectoral fin propulsion system, also known as an undulating-fin system, is introduced, reducing the robot's size and weight while enabling effective locomotion in both aquatic and terrestrial settings. Additionally, a combined propulsion system integrating undulating fins with dual caudal fins is developed to improve underwater propulsion efficiency further. The performance of the proposed design is evaluated through fluid dynamics analyses and validated with real-world experiments, demonstrating superior swimming speeds, enhanced underwater maneuverability, and versatile motion gaits compared to single propulsion modes. The robot achieves a minimum Cost of Transport of 3.25 for aquatic locomotion and 5.08 for terrestrial locomotion, outperforming several existing amphibious robots. These advancements highlight the valuable insights for the development of efficient and versatile amphibious robots.

Keywords: Amphibious Robot, Biomimetic Design, Undulating Fin,

*Corresponding author. E-mail address: yongxiajia@tsinghua.edu.cn (Yongxia Jia), hwx@tsinghua.edu.cn (Weixi Huang), xiegm@pku.edu.cn (Guangming Xie).

¹This is the first author footnote.

1. Introduction

Amphibious robots represent an advanced class of robotic platforms capable of operating effectively across diverse environments, enabling seamless transitions between land and water (Nygaard et al., 2021; Ren and Yu, 2021). These robots are designed to perform a wide range of tasks in various settings such as land, coastal zones, and complex underwater environments (Bai et al., 2022; Shah et al., 2021). Different environments possess distinct characteristics, attributes, and surface types for robotic operation. Moreover, transitioning between environments with identical designs remains a challenging issue. These complexities open up new technical problems, dimensions, and research areas for exploration (Rafeeq et al., 2021).

In the design of amphibious robots, biomimetic approaches have gained widespread acceptance due to their practical potential for development and deployment. Certain animals have attracted considerable research attention due to their remarkable flexibility, adaptability, and mobility across land and water. The turtle is a classic amphibious organism, with four paddle-shaped limbs: forelimbs serve as paddles and hind limbs function as rudders (Duellman and Trueb, 1994). Typical sea turtle-inspired robots include spherical designs (Guo et al., 2018; Li et al., 2017; Xing et al., 2018), tortoise-inspired soft robots (Wu et al., 2022), and the Yale ART (Baines et al., 2022), all exhibiting good maneuverability. Crab-inspired robots, which move on land or crawl in both terrestrial and aquatic environments (Graf et al., 2019; Shim et al., 2016), have also been developed. Some models draw inspiration from the fiddler crab, with flat, oar-shaped appendages for underwater movement (Chen et al., 2022; Wang et al., 2017). Cockroach-inspired robots, such as AmphiHex-I (Zhang et al., 2016) and AmphiHex-II (Zhong et al., 2018), achieve amphibious locomotion using leg-based movement, demonstrating excellent maneuverability and multi-terrain adaptability. Snake-inspired robots navigate both land and water via undulating or rolling motion (Milana et al., 2020; Ohashi et al., 2010), with some incorporating wheels to assist on land (Yu et al., 2012). Frog-inspired amphibious robots employ various drive mechanisms, such as the hybrid movement of the FroBot, which combines frog swimming and scooter motion (Yi et al., 2015), and a design by Yang et al. (Yang et al., 2024) that integrates frog and mudskipper movements for amphibious locomotion.

Notably, biomimetic amphibious robots inspired by stingrays have been developed, leveraging the pectoral fins (also known as undulating fins) for land propulsion (Filardo et al., 2020; Xia et al., 2023). Due to the high maneuverability of undulating fins (Kato, 2005), stingray-inspired robots are particularly well-suited for navigating complex environments and performing a wide range of tasks effectively, compared to other biomimetic amphibious robots. However, existing designs often involve actuating each fin ray with an individual servo motor, requiring numerous servos—sometimes exceeding a dozen. Moreover, these robots include mechanisms to adjust the angle of the undulating fins: the fins are positioned at a 90° angle to the horizontal plane during terrestrial locomotion and parallel to it during aquatic locomotion. These complexities result in large, cumbersome, and energy-intensive robots, ultimately limiting propulsion efficiency across different environments.

To address these challenges, we propose a design approach to enhance the propulsion efficiency of stingray-inspired amphibious robots. First, we introduce an efficient undulating-fin propulsion system, where a single servo controls each fin, reducing the total number of servos to only two. Additionally, the fins are fixed at a slightly downward-tilted angle, enabling seamless locomotion in both aquatic and terrestrial environments without the need for angle adjustments. This design reduces the robot’s weight and servo count, thereby improving propulsion efficiency.

Furthermore, many aquatic animals use a combination of pectoral and caudal fins to enhance underwater propulsion efficiency. For instance, species like the black surfperch and bluegill sunfish rely on pectoral fins for low-speed swimming but engage both pectoral and caudal fins at higher speeds (Drucker and Lauder, 2000). Studies have shown that this coordinated use of pectoral and caudal fins enhances propulsion efficiency (Han et al., 2020; Mignano et al., 2019), maneuverability (Lin et al., 2023), and stability (Qiu et al., 2023). Inspired by these findings, we incorporated caudal fins into our design to further improve the robot’s underwater propulsion efficiency.

To validate and optimize the proposed design, we employed Particle Image Velocimetry (PIV) experiments (Liu and Curet, 2018; Piskur, 2022a) and Computational Fluid Dynamics (CFD) simulations (Costa et al., 2017; Yue et al., 2013), both of which are widely used for underwater robotic analysis. The performance of our system, particularly the incorporation of caudal fins into the design, was evaluated using these methods. Additionally, real-world experiments were conducted to collect motion data and further validate the system’s capabilities.

The paper is organized as follows. Section 2 outlines the design of the amphibious robot. Section 3 focuses on the locomotion analysis, where we develop a locomotion model, followed by a discussion on the implementation of locomotion. This section also explores flow dynamics, drawing insights from both PIV experiments and CFD simulations. Section 4 presents the experimental results, and Section 5 concludes the paper and discusses potential directions for future work.

2. Design of the Amphibious Robot

The design of the robot is systematically segmented into two major components: the main body and the propulsion system, as depicted in Fig. 1(a). In the following sections, we will provide a detailed description of design of each components.

2.1. Design of the Robot Main Body

The main body of robot consists of a streamlined head and a flat body, designed to reduce drag. The head’s outer shell, 3D printed using transparent photopolymer resin, houses an infrared obstacle avoidance module and a camera module. The electronics within the head are connected to the battery and Arduino board via an aerial plug located at the front of the body, as shown in Fig. 1(b). Additionally, two waterproof servo slots are positioned on each side of the head, each housing a servo that controls the undulating fins.

The body, 3D printed using photopolymer resin, features a box-type design with a detachable sealing cover on top, providing convenient access to internal circuits for debugging. To ensure waterproofing, a static seal is implemented using a 1 cm wide groove fitted with a silicone gasket. The cover is secured to the body edges with screws, ensuring an effective seal. As shown in Fig.1(e), the Arduino board, battery, and breadboard are neatly arranged within the body. For safety, the power switch is mounted externally above the body. Additionally, Fig.1(d) illustrates the supporting structures on both sides of the box, which prevent bending and deformation of the rotating rod, ensuring the stability of the undulating-fin propulsion system.

2.2. Design of the Propulsion Systems

In the undulating-fin propulsion system, the driving mechanism and the shape of the undulating fin surface are meticulously designed to achieve active wave-like motion of the fin.

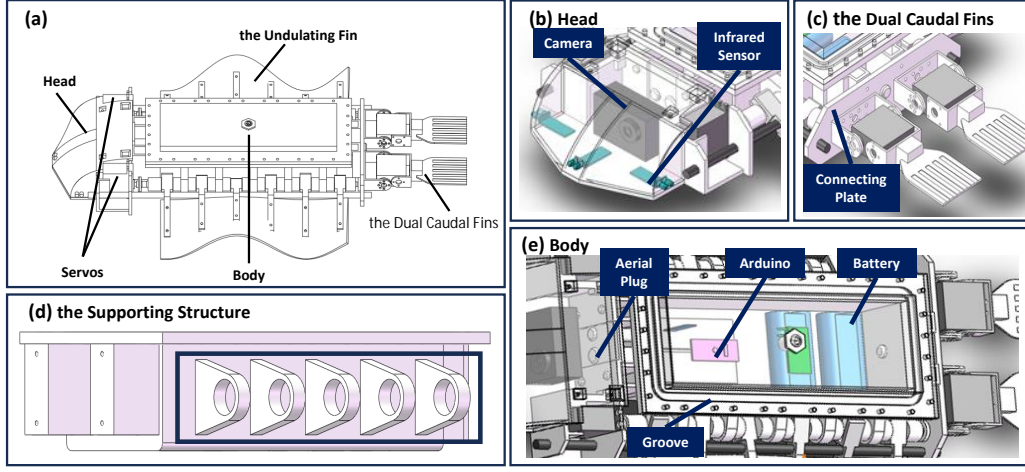


Fig. 1: (a) Overview of the robot design. (b) Detailed view of the head of the robot, showing sensory components and internal structure. (c) Model of the dual caudal fins with a detailed view of the connection between the body and caudal fins. (d) Illustration of the support structure providing stability for the undulating-fin propulsion system. (e) Model of the robot body, displaying the internal layout.

For the undulating fin, a 3 mm thick silicone sheet was selected based on material testing, offering a balance between flexibility for undulation and rigidity for terrestrial locomotion. The fin has a two-dimensional fan-shaped surface that bends to create a three-dimensional undulating motion. The design parameters of the undulating fin are shown in Fig.2(a). Point A represents the center of the rotating rod, point B the center of the fixed rod, and point C the outermost point of the fin surface. The wave height, h , refers to the vertical displacement of the outer fin surface relative to the fixed rod. The eccentricity of the rotating rod is e , the distance between the fixed and rotating rods is l , and the rotation angle of the eccentric rotating rod is θ . The inner arc diameter is denoted by R , the width by d , and the arc angle by α . The wavelength λ of the outer edge of the undulating fin is defined as $\lambda = R\alpha$. Using Eq.1, the wave height h can be calculated as follows:

$$h(\theta) = \frac{ed \sin \theta}{\sqrt{e^2 + l^2 - 2el \cos \theta}} \quad (1)$$

The outer fin surface waveform, calculated using $h(\theta)$ and shown in Fig. 2(b), closely approximates a sine wave. This suggests that we can adopt the sinusoidal model proposed by Yin et al. (Yin et al., 2021) for fabricat-

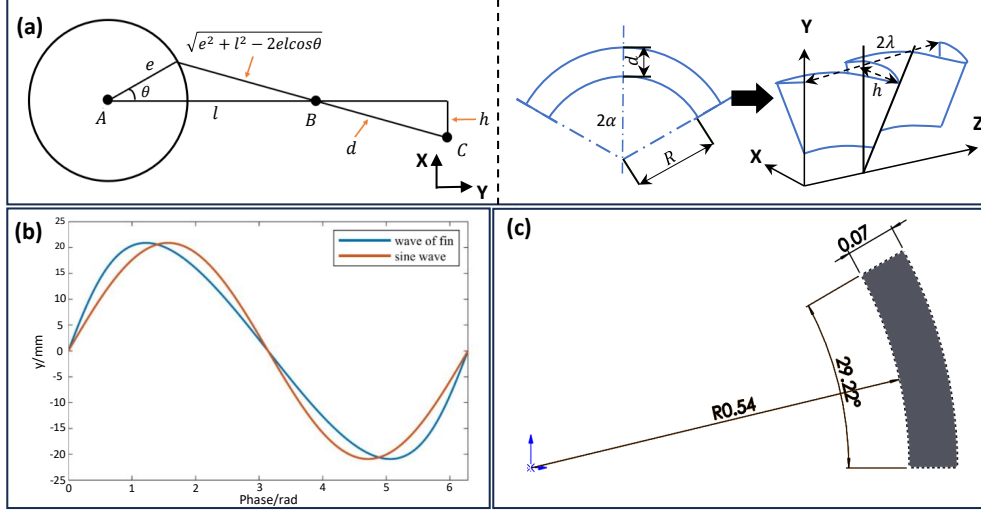


Fig. 2: (a) Schematic of undulating fin parameters. (b) Comparison of the actual wave shape h along the outer fin surface with sine wave, highlighting their similarity. (c) Final schematic of the undulating fin surface, showing the calculated parameters and refined shape.

ing our undulating fin. In this model, the length of the sinusoidal curve is equivalent to the length of the outer arc, as defined by the following equation:

$$\int_0^{\frac{R\alpha}{4}} \sqrt{1 + \left(\frac{2\pi h}{R\alpha} \cos \left(\frac{4\pi}{R\alpha} z \right) \right)^2} dz = \frac{\alpha(R + d)}{4} \quad (2)$$

By applying this equation along with the structural parameters, the precise dimensions of the arc-shaped undulating fin can be determined. The final design of the fin surface is shown in Fig. 2(c).

The mechanism driving the wave-like motion of the undulating fin is composed of three primary components: the rotating rod, the fin rays, and the fixed rod. The rotating rod is connected to a waterproof servo at the front and secured to the connecting plate via a bearing at the rear. The middle section of the rotating rod is composed of seven segments, with adjacent segments linked by off-center circular rods (3 mm radius) that create a 90° phase difference between each pair, as shown in Fig.3(a). This design allows the entire fin surface to move in a wave-like motion, generated by the fixed phase difference between the fin rays, facilitating efficient propulsion. The forked fin rays are attached at one end to the off-center rods and at the

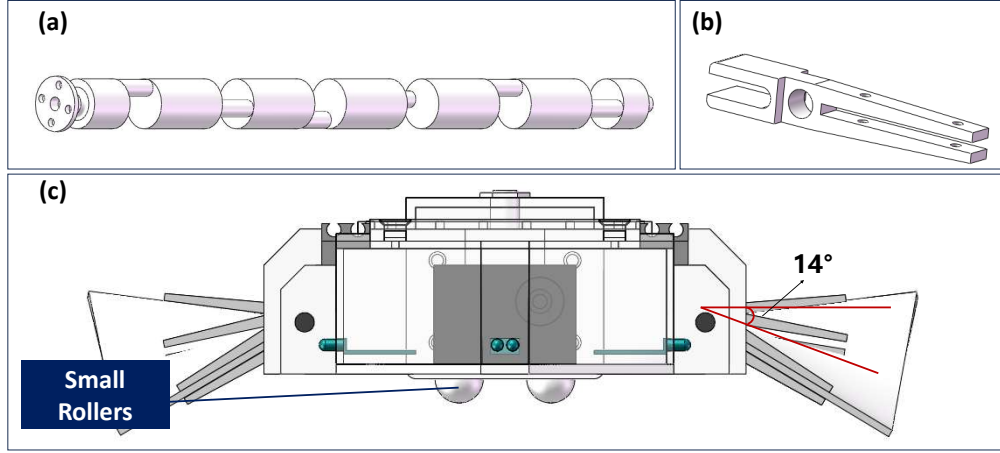


Fig. 3: (a) Diagram of the rotating rod structure driving the undulating fins. (b) Close-up of the fin rays, highlighting the forked design. (c) Front view of the body, showing the placement of the undulating fins relative to the body and the position of the four small rollers.

other to the fin surface (Fig.3(b)). A central hole in the fin rays allows the carbon fiber fixed rod to pass through, providing added stability as it extends through the robot's head and the connecting plate. By using a single servo to control the entire fin surface, this design eliminates the need for individual servos for each fin ray, reducing both weight and power consumption. The phase difference between the rod segments generates a coordinated wave motion, enabling efficient propulsion.

To achieve seamless locomotion across both aquatic and terrestrial environments, we fixed the undulating fins at a slightly downward-tilted angle, achieved by setting the fixed and rotating rods at different heights. We selected a 14° downward tilt for our robot, which allows the fins to make contact with the ground during terrestrial locomotion without significantly affecting underwater performance. In addition, four small rollers placed beneath the robot's body reduce ground resistance by converting sliding friction into rolling friction, thereby enhancing speed (Fig. 3(c)). This design enables the robot to transition between water and land without the need for angle adjustments.

The caudal-fin propulsion system, inspired by the grouper, features a flat shape designed to prevent interference between the two fins. The side-by-side caudal fins are 3D printed using photopolymer resin, ensuring precise

and durable construction. Given the bending modulus of the photopolymer resin material (2178–2222 MPa), the elasticity of the caudal fins is considered negligible, and their stiffness is assumed to remain constant during swimming. The fins are connected to waterproof servos via servo brackets, with the servos mounted on a connecting plate at the rear of the robot, as shown in Fig. 1(c).

3. Locomotion Analysis of the Robot

3.1. Locomotion Model

3.1.1. Coordinate System Setup

To analyze the kinematics and dynamics of the robot, two coordinate systems are defined. The first is a global coordinate system (X_0 - Y_0 - Z_0), which serves as the fixed inertial frame of reference. The second is a body-fixed coordinate system (X - Y - Z), rigidly attached to the robot and moving with it. The body-fixed coordinate system uses the primary component of the robot, excluding the undulating and caudal fins, as its reference base, as this component is modeled as a rigid body. The origin of the body-fixed coordinate system is located at the center of mass of the entire body.

The orientation of the body-fixed coordinate system is defined as follows: the positive Z -axis points toward the front of the robot, the positive X -axis aligns with the top of the body, and the positive Y -axis is determined using the right-hand rule. This configuration is illustrated in Fig. 4(a).

3.1.2. Kinematic Analysis

The kinematics analysis on the robot has been performed according to the above body-fixed coordinate system. Within which the caudal fins flap and undulating fins fluctuate in place. Due to the symmetry of the body, it is adequate to focus on one side of the undulating fins and caudal fins.

$$\begin{cases} x = A \sin \theta(t) \\ y = A \cos \theta(t) \\ \theta = \theta_0 \sin(\omega t + kz + \varphi) \end{cases} \quad (3)$$

where the amplitude A is proportional to the perpendicular distance from a point on the fin surface to the root of the fin, being 0 at the fin root and equal to the fin width at the fin tip. The angular amplitude θ_0 , angular frequency ω , wave number k , and initial phase φ are defined as the key parameters of the wave function.

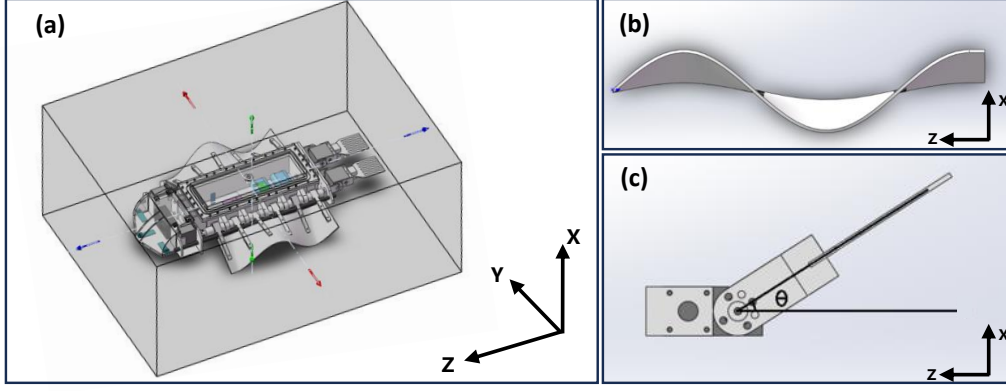


Fig. 4: (a) Schematic of the body-fixed coordinate system. (b) Side view of the undulating fin with a sinusoidal profile in the Z - X plane. (c) Side view of the caudal fin, rotating around a fixed axis at angle θ .

The caudal fin can be treated as a rigid body rotating around a fixed axis, with its position determined by a single variable, the angle θ between the fin surface and the Y - Z plane, as illustrated in Fig. 4(c). Subsequently, the position of the caudal fin at each moment can be obtained by integrating the angular velocity of the servo over time:

$$\theta(t) = \theta_0 + \int_0^t \omega(t) dt \quad (4)$$

where θ_0 represents the initial position of the caudal fin, and $\omega(t)$ is the function describing the rotational velocity.

3.1.3. Hydrodynamic Analysis

The analysis is conducted within a body-fixed coordinate system (X - Y - Z), where the force balance considers the interaction between external hydrodynamic forces and inertial forces.

The propulsion of the robot is generated by the interaction between the undulating fins, caudal fins, and the surrounding water. During swimming, the undulating fins create a backward-propagating wave along the robot's body, generating forward thrust. Theoretical models, such as Lighthill's elongated body theory (Sir James, 1975) and Tong's three-dimensional undulating plate theory (Sir James, 1975; Tong et al., 1991), predict that forward motion occurs when the wave speed (c) exceeds the swimming speed (u).

For the caudal fins, propulsion arises from the generation of reverse Kármán vortex streets, which create reactive forces driving the robot forward.

3.1.4. Dynamics Modeling

The robot consists of five primary components: the main body, dual undulating fins, and dual caudal fins. In the following analysis, we focus solely on the motion of the main body, while the other four components are simplified as a power source and resistance. However, when calculating the mass and rotational inertia of the robot, these components are included in the assessment. The subsequent discussion provides a rigid-body dynamics analysis of the main body.

Consider the mass of the main body as m_1 , the mass of a single undulating fin as m_2 , and the mass of a single caudal fin as m_3 . The positions of the center of mass for the main body, the overall center of mass for the two undulating fins, and the overall center of mass for the two caudal fins are denoted as \mathbf{r}_1 , \mathbf{r}_2 and \mathbf{r}_3 , respectively, in the global coordinate system X_0 - Y_0 - Z_0 . The robot center of mass position can be determined using the following equation:

$$\mathbf{r}_c = \frac{\mathbf{r}_1 m_1 + 2\mathbf{r}_2 m_2 + 2\mathbf{r}_3 m_3}{m_1 + 2m_2 + 2m_3} \quad (5)$$

The forces acting on each part of the robot include: gravity of the main body \mathbf{G} , buoyancy of the main body \mathbf{F} , drag of the main body (both chordal and lateral) \mathbf{R} , normal force of the undulating fins (defined as the vector sum of gravity and buoyancy) \mathbf{P}_1 , normal force of the caudal fins \mathbf{P}_2 , net propulsive force of the undulating fins (defined as the vector sum of the propulsive force and the drag force) \mathbf{T}_1 , and net propulsive force of the caudal fins \mathbf{T}_2 . For a robot swimming horizontally in water, there exists a kinetic equation in a global coordinate system, as shown in Eq. 6:

$$\begin{cases} \mathbf{F} = \mathbf{G} + \mathbf{P}_1 + \mathbf{P}_2 \\ (m_1 + 2m_2 + 2m_3) \ddot{\mathbf{r}}_c = \mathbf{T}_1 + \mathbf{T}_2 - \mathbf{R} \end{cases} \quad (6)$$

The second equation above can be written in component form:

$$\begin{cases} \ddot{X}_C = 0 \\ (m_1 + 2m_2 + 2m_3) \ddot{Y}_C = T_{1y} + T_{2y} - R_y \\ (m_1 + 2m_2 + 2m_3) \ddot{Z}_C = T_{1z} + T_{2z} - R_z \end{cases} \quad (7)$$

3.2. Implementation of Locomotion

(a) Linear motion

In water, the robot exhibits four distinct gaits of forward motion. The first pattern utilizes the undulating fins, which generate backward-propagating waves that create forward propulsion. In the second pattern, the dual caudal fins move synchronously without any phase difference. In the third pattern, the dual caudal fins operate with a half-cycle phase difference, generating a steady forward thrust. Lastly, in the combined swimming mode, the undulating fins provide primary forward thrust while the dual caudal fins, operating half a cycle out of phase, enhance the thrust and increase the robot's linear speed. For backward motion in water, the undulating fins reverse their action, producing forward-propagating waves that propel the robot in the opposite direction.

On land, locomotion is achieved solely through the undulating fins. During forward movement, the fins generate forward-propagating waves, creating friction against the ground to drive the robot forward. Conversely, backward-propagating waves are used for reverse motion, enabling the robot to move backward.

(b) Acceleration Motion

As described in Eqs. 6 and 7, the robot accelerates from a stationary state due to the thrust generated by its propulsion systems. With increasing velocity, the body experiences growing resistance, \mathbf{R} , which eventually balances the thrust, allowing the robot to reach and maintain a steady-state speed. Upon cessation of propulsion, the thrust diminishes, and the robot decelerates under the influence of drag until it comes to a complete stop.

To expedite deceleration in water, the undulating fins reverse their motion, generating forward-directed surface waves that enhance drag. Additionally, the phase angle θ of the dual caudal fins is set to $-\pi/2$, further increasing resistance and improving braking performance.

(c) Turning Motion

In water, the robot achieves turning motion through three distinct gaits enabled by the asymmetrical operation of the undulating fins or caudal fins. In the first pattern, the undulating fins move in opposite directions, allowing the robot to turn on-site. The turning radius can be adjusted by varying the speed of the fins. In the second pattern, the caudal fins operate with a quarter-cycle phase difference, creating asymmetric thrust that generates torque for steering. In the third pattern, during linear propulsion with the

undulating fins, the dual caudal fins are positioned 180° apart to function as rudders, producing additional torque to facilitate turning.

On land, the robot performs turns by adjusting the undulating fins to move in opposite directions, creating forces for steering.

3.3. Flow Dynamics

To evaluate the performance of our system, particularly the incorporation of caudal fins into the design, we employed PIV experiments and CFD simulations. Below, we provide a detailed explanation of the PIV experimental setup and the numerical model used in the CFD simulations, followed by an analysis of the obtained results.

3.3.1. PIV Experiment

We conducted PIV experiments for the undulating-fin swimming mode and the caudal-fin swimming mode. Given the symmetry of the robot about the Z - X plane, the undulating fin and caudal fin on one side were needed for the PIV experiments, as shown in Fig.5(a).

The experiments were performed in a low-turbulence water channel (Fig.5(b)), with a test section measuring 2 m in length, 0.4 m in width, and 0.5 m in height, allowing flow speeds to be adjusted up to 0.6 m/s. The incoming flow velocity was set at $v_0 = 0.172$ m/s. For flow field measurements, a PIV system (LaVision Int, Germany) was employed (Fig. 5(c)), consisting of a high-speed CMOS camera, a 30 mJ pulsed laser, a data acquisition and analysis software. Tracer particles with a diameter of $10\ \mu\text{m}$ were employed to visualize the flow. During the experiments, the robot model was fixed in the test section, and the camera captured images at 300 frames per second, synchronized with the laser frequency. For velocity calculations, a 32×32 pixel interrogation window was used, with a 75% overlap between adjacent windows.

3.3.2. CFD Simulation

For CFD simulation, a towing model is employed where the robot remains stationary while the fluid flows past it with a constant incoming velocity. During the swimming process, the undulating and caudal fins generate all the thrust and a small portion of the drag, whereas the main body contributes the majority of the drag. To focus on the thrust differences among various propulsion modes, the body is simplified to a rectangular box in the CFD simulations. However, the undulating fins and caudal fins are modeled

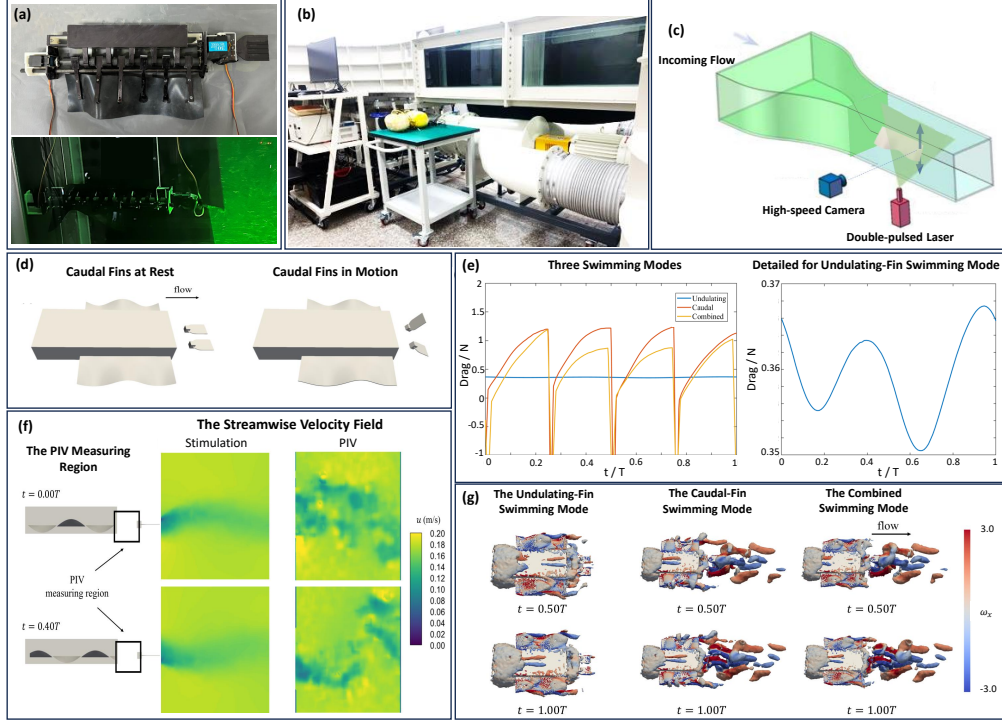


Fig. 5: (a) Setup of the robot model for PIV experiments. (b) Low-turbulence water channel used for the experiments. (c) Schematic of the PIV experimental design and measurement setup. (d) The robot model used in fluid dynamics simulations, showing different caudal fin movement states. (e) Variation of total drag force over one cycle for three swimming modes, as obtained from CFD simulations. (f) Measurement region for the PIV experiments, along with streamwise velocity fields for the undulating-fin swimming mode obtained from both PIV experiments and CFD simulations. (g) Vortical structures of the robot across the three swimming modes, visualized using $Q = 1$ isosurfaces and colored by the streamwise vorticity ω_x .

with their precise dimensions and shapes, maintaining the relative positioning of all components. For the undulating-fin swimming mode, the caudal fins remain horizontal and stationary, and the undulating motion of the fin surface is described by Eq. 3. In the caudal-fin swimming mode and the combined swimming mode, the dual caudal fins operate with a half-cycle phase difference. As shown in Fig. 5(d).

The robot model is positioned within a sufficiently large computational domain to ensure that boundary effects do not influence the flow around the

model. A constant velocity condition is applied at the inlet, and a constant pressure condition is set at the outlet, while the boundaries of the domain and the surface of the model are treated as no-slip. The Reynolds-Averaged Navier-Stokes equations are employed to compute the velocity and pressure fields, with the Reynolds stresses determined using the $k-\omega$ SST model. The motions of the undulating and caudal fins are simulated using the dynamic mesh method, where the mesh deforms with the movement of the fins and is smoothed or remeshed as necessary at each time step.

Simulations are conducted for three swimming modes (undulating-fin, caudal-fin, and combined swimming modes) at the same incoming flow velocity of $u_0 = 0.172$ m/s. The undulating fins are set to a frequency of 1.9 Hz, while the caudal fins operate at a frequency of 0.8 Hz. The wavelength of the undulating fins is $\lambda = 18.4$ mm, and each fin contains one and a half wavelength.

3.3.3. PIV and Simulation Results

In the undulating-fin swimming mode, the velocity fields behind the fins, obtained from both PIV experiments and CFD simulations, are presented in Fig. 5(f). This comparison serves to validate the accuracy of the CFD model. Specifically, tip vortices shed by the undulating fins create low-speed streaks in the wake, which are clearly observed in both the PIV and CFD results. The consistency between the experimental and simulation data confirms that the CFD simulations accurately capture the flow structures observed in the PIV experiments. This agreement provides confidence in using CFD for further flow analysis under varying conditions.

Fig. 5(e) shows the time histories of the drag force obtained from CFD simulations across three swimming modes. In the undulating-fin swimming mode, the drag force exhibits a sinusoidal pattern, with two peaks per undulation cycle. Due to the relatively small amplitude of the undulation, the fins undergo slight deformation, resulting in stable drag fluctuations and a steady swimming motion. In contrast, in the caudal-fin swimming mode, the drag force displays four minima per cycle, corresponding to the moments when the caudal fins reverse direction, generating substantial thrust. In the combined swimming mode, the drag force variation is similar to that in the caudal-fin swimming mode, with four minima per cycle; however, the average drag is lower than in the caudal-fin swimming mode. This suggests a synergistic effect between the undulating and caudal fins that enhances propulsion efficiency. These CFD results provide a deeper understanding of the drag dy-

Table 1: Prototype Parameters of the Robot

Parameters	Unit	Value (s)
Body Length	mm	602
Overall Width	mm	413
Body Height	mm	95
Total Weight	kg	2.67
Torque of Caudal Fins' Servo	kg-cm	30
Torque of Undulating Fins' Servo	kg-cm	40
Capacity of Battery	mAh	1500
Battery Voltage	V	7.4
Robot Endurance	min	55
Remote Control Distance (Bluetooth)	m	3

namics across different swimming modes and further support the hypothesis that the combined use of both fin types enhances overall propulsion.

Fig. 5(g) illustrates the vortical structures using the Q -criterion (Hunt et al., 1988). Tip vortices are observed consistently on the fins across all three swimming modes. When the undulating fins are stationary, vortices form at the wave crests and troughs, extending along the flow direction and contributing to drag. Upon initiating undulation, these vortices decrease in size and become confined to the edges, thereby reducing the low-pressure drag effect. Additionally, trailing-edge vortices generated by the caudal fins form a reverse Kármán vortex street, which enhances thrust. These observations further support the conclusion that the combined action of both fin types enhances propulsion performance by improving thrust generation and reducing drag.

4. Experimental Testing and Validation

4.1. Testing Methods and Procedures

The specific parameters of the robot are shown in Table 1. Underwater movement tests were conducted in a pool with dimensions of 3.5 m \times 2 m \times 0.6 m. For terrestrial movement, the experiments were carried out on ceramic tiles. A video camera was positioned adjacent to the testing area to capture and record the movements, enabling detailed data analysis.

Before the underwater tests, the robot underwent waterproofing and weight adjustment. After these preparations, it was placed in a pool, where

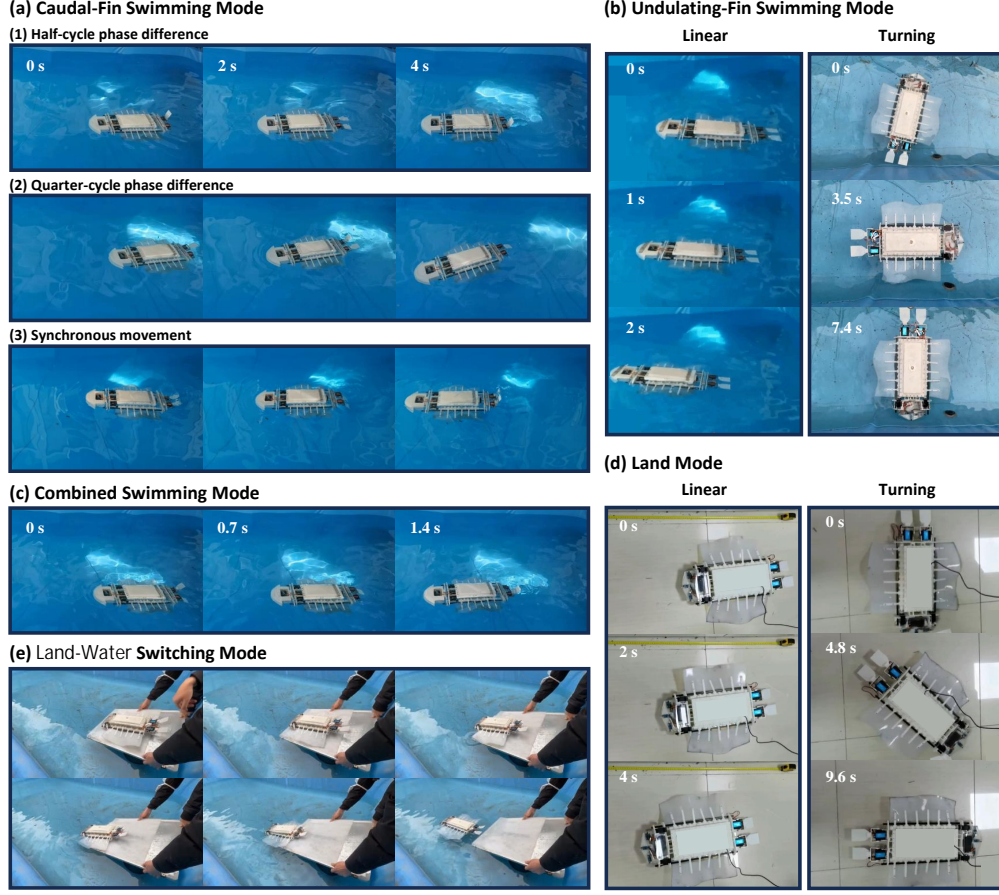


Fig. 6: (a) The robot performs a variety of movements by adjusting the phase difference between the dual caudal fins. (b) Linear and turning motions in the undulating-fin swimming mode. (c) Linear motion in the combined swimming mode. (d) Linear and turning motions in the land mode. (e) Transition between land and water locomotion.

it was controlled via software to perform various motion modes. The tests included linear and turning movements in three propulsion modes: undulating-fin, caudal-fin, and combined swimming modes. Linear speed, turning speed, and turning radius were estimated through video analysis.

For land movement testing, the dual caudal fins were deactivated, and the robot performed linear and turning motions by adjusting the undulating frequency of the fins. The experiments also explored land-to-water transitions using an inclined wooden board covered with a silicone sheet, positioned next to the pool.

4.2. Experimental Results

In the experiment, the propulsion efficiency was evaluated using the cost of transport (COT) (Baines et al., 2022; Kuo, 2007), a key metric for motion efficiency. COT quantifies the energy consumed for the robot to travel a given distance, normalized by its weight. It is computed using the average input power, $\overline{P_{\text{in}}(t)}$, as follows:

$$\text{COT} = \frac{\overline{P_{\text{in}}(t)}}{mg \cdot \overline{v_{\text{bot}}}} \quad (8)$$

where m is the mass of the robot, g is the local gravitational acceleration, and $\overline{v_{\text{bot}}}$ is the average speed of robot during the test. The input power, $\overline{P_{\text{in}}(t)}$, is the sum of the average power consumed by all four servos, measured using a power measurement module (Model INA226):

$$\overline{P_{\text{in}}(t)} = \sum_{i=1}^4 \overline{I_i(t)} V \quad (9)$$

where $\overline{I_i(t)}$ is the average current drawn by the i -th servo, and $V = 7.4$ V is the supply voltage. This approach allows accurate estimation of total power input based on real-time measurements of the servo’s electrical consumption.

The efficiency of the robot was assessed by measuring linear speed and COT for both underwater and land locomotion across various actuation frequencies, with the results summarized in Table 2. The robot is also capable of transitioning between water and land locomotion, as shown in Fig. 6(e), illustrating the seamless transition enabled by our design. Furthermore, while the caudal-fin swimming mode has a turning radius of 4.6 m, both the combined and undulating-fin swimming modes can perform on-site turns at a speed of 23.08 °/s. Additionally, the land mode allows for on-site turning at a speed of 9.32 °/s.

The experimental results show that, at the same actuation frequency, the combined swimming mode achieves a 40% higher speed than the undulating-fin swimming mode. Additionally, within the tested speed range, the COT of the undulating-fin swimming mode increases with speed, exhibiting a strong linear relationship ($R^2 = 0.9941$). Based on this, we estimate that when the speed of the undulating-fin swimming mode reaches 0.14 m/s (the same speed as the combined swimming mode), its COT would be 3.64. Therefore, at equivalent speeds, the combined swimming mode demonstrates superior

Table 2: Experimental Results of Linear Speed and COT for Underwater and Land Locomotion

Mode	Undulating-Fin Frequency (Hz)	Caudal-Fin Frequency (Hz)	Linear Speed (m/s)	COT
The Undulating-Fin Swimming Mode	1.25	0	0.08	2.75
	1.43	0	0.09	2.88
	1.67	0	0.10	3.05
The Caudal-Fin Swimming Mode	0	1	0.05	5.61
The Combined Swimming Mode	1.67	1	0.14	3.25
The Land Mode	1.67	0	0.06	5.08

energy efficiency, consuming 10.7% less energy than the undulating-fin swimming mode.

Our robot achieves a minimum COT of 3.25 for aquatic locomotion and 5.08 for terrestrial movement, outperforming several amphibious robots (Baines et al., 2022) and even advanced unimodal robots. For example, it outperforms terrestrial peristaltic crawling robots like earthworm-like robots by ten times (A et al., 2021), and terrestrial legged robots, such as the MIT learning biped by six times (Kuo, 2007) and TITAN-XIII (Kitano et al., 2016) by two times. In aquatic environments, it outperforms various specialized robots, including the dielectric elastomer actuator robotic jellyfish by ten times, the Finbot by three times (Berlinger et al., 2021), and demonstrates performance comparable to the energy-efficient underwater robot Tunabot (White et al., 2021). These comparisons highlight the propulsion efficiency advantages of our robot and emphasize its potential for practical applications.

5. Conclusions

This study presents a novel design approach to enhance the propulsion efficiency of stingray-inspired amphibious robots. First, an innovative undulating-fin propulsion system was developed, where a single servo controls the entire fin on each side, enabling seamless locomotion across both

aquatic and terrestrial environments without the need for angle adjustments. Additionally, caudal fins were incorporated into the design to further improve underwater propulsion efficiency. To evaluate the performance of our system, particularly the incorporation of caudal fins into the design, we employed PIV experiments and CFD simulations. Real-world experiments confirmed that the combined swimming mode outperforms both the undulating-fin and caudal-fin swimming modes when used independently, delivering superior propulsion efficiency (as measured by COT), enhanced maneuverability, and adaptability across various movement gaits.

Compared to existing amphibious and advanced unimodal robots, our robot achieves a minimum COT of 3.25 for aquatic locomotion and 5.08 for terrestrial locomotion, showcasing its superior propulsion efficiency. These results demonstrate the potential of the proposed propulsion system to enhance energy efficiency and position our robot as a competitive solution for operation in diverse and challenging environments.

The robot’s enhanced propulsion efficiency and maneuverability make it suitable for a wide range of challenging applications, including resource exploration, ecological monitoring, and environmental surveying. The versatility of the propulsion system allows it to adapt to diverse operational conditions, broadening the scope of potential real-world applications for amphibious robots.

Despite promising results, several areas remain for future improvement. To enhance the robot’s capabilities, future work will focus on expanding its movement gaits by incorporating buoyancy control for diving and resurfacing. The current experimental tests were conducted within a limited speed range, and further optimization is needed for better performance, particularly in dynamic environments and rugged terrestrial terrains. Additionally, the elasticity of the caudal fins, a critical factor in biomimetic propulsion systems (Paifelman et al., 2024; Piskur, 2022b; Wang et al., 2023), requires further investigation. The current design of the caudal fins using rigid materials may limit their performance, and future efforts will focus on incorporating elastic materials to improve propulsion efficiency and overall functionality. In summary, these improvements will enhance the robot’s versatility, performance, and real-world applicability, making it better suited for practical use across a wider range of environments.

Acknowledgment

The authors would like to extend their sincere gratitude to Limu Wang, Xijie Mei, and Xinyu Tang for their invaluable assistance in the design and simulation of the robot throughout this project. Their expertise and support have been instrumental in the successful completion of this work.

This work was supported by the National Natural Science Foundation of China under Grant Nos. 12272008, 12425206, 92252204 and 12272206.

References

- A, K., Y, W., Hj, C., Rd, Q., Ka, D., 2021. An Analysis of Peristaltic Locomotion for Maximizing Velocity or Minimizing Cost of Transport of Earthworm-Like Robots. *Soft robotics* 8. doi:10.1089/soro.2020.0021.
- Bai, X.j., Shang, J.z., Luo, Z.r., Jiang, T., Yin, Q., 2022. Development of amphibious biomimetic robots. *Journal of Zhejiang University-SCIENCE A* 23, 157–187. doi:10.1631/jzus.A2100137.
- Baines, R., Patiballa, S.K., Booth, J., Ramirez, L., Sipple, T., Garcia, A., Fish, F., Kramer-Bottiglio, R., 2022. Multi-environment robotic transitions through adaptive morphogenesis. *Nature* 610, 283–289. doi:10.1038/s41586-022-05188-w.
- Berlinger, F., Saadat, M., Haj-Hariri, H., Lauder, G.V., Nagpal, R., 2021. Fish-like three-dimensional swimming with an autonomous, multi-fin, and biomimetic robot. *Bioinspiration & Biomimetics* 16, 026018. doi:10.1088/1748-3190/abd013.
- Chen, X., Li, J., Hu, S., Han, S., Liu, K., Pan, B., Wang, J., Wang, G., Ma, X., 2022. Study on the Design and Experimental Research on a Bionic Crab Robot with Amphibious Multi-Modal Movement. *Journal of Marine Science and Engineering* 10, 1804. doi:10.3390/jmse10121804.
- Costa, D., Franciolini, M., Palmieri, G., Crivellini, A., Scaradozzi, D., 2017. Computational fluid dynamics analysis and design of an ostraciiform swimming robot, in: 2017 IEEE International Conference on Robotics and Biomimetics (ROBIO), pp. 135–140. doi:10.1109/ROBIO.2017.8324407.

- Drucker, E.G., Lauder, G.V., 2000. A Hydrodynamic Analysis of Fish Swimming Speed: Wake Structure and Locomotor Force in Slow and Fast Labriform Swimmers. *Journal of Experimental Biology* 203, 2379–2393. doi:10.1242/jeb.203.16.2379.
- Duellman, W.E., Trueb, L., 1994. *Biology of Amphibians*. JHU Press.
- Filardo, B.P., Zimmerman, D.S., Weaker, M.I., 2020. Vehicle with Traveling Wave Thrust Module Apparatuses, Methods and Systems.
- Graf, N.M., Behr, A.M., Daltorio, K.A., 2019. Crab-Like Hexapod Feet for Amphibious Walking in Sand and Waves, in: *Biomimetic and Biohybrid Systems*, Springer International Publishing. pp. 158–170. doi:10.1007/978-3-030-24741-6_14.
- Guo, S., He, Y., Shi, L., Pan, S., Xiao, R., Tang, K., Guo, P., 2018. Modeling and experimental evaluation of an improved amphibious robot with compact structure. *Robotics and Computer-Integrated Manufacturing* 51, 37–52. doi:10.1016/j.rcim.2017.11.009.
- Han, P., Lauder, G.V., Dong, H., 2020. Hydrodynamics of median-fin interactions in fish-like locomotion: Effects of fin shape and movement. *Physics of Fluids* 32, 011902. doi:10.1063/1.5129274.
- Hunt, J.C.R., Wray, A.A., Moin, P., 1988. Eddies, streams, and convergence zones in turbulent flows. *center for turbulence research*.
- Kato, N., 2005. Median and Paired Fin Controllers for Biomimetic Marine Vehicles. *Applied Mechanics Reviews* 58, 238–252. doi:10.1115/1.1946027.
- Kitano, S., Hirose, S., Horigome, A., Endo, G., 2016. TITAN-XIII: sprawling-type quadruped robot with ability of fast and energy-efficient walking. *ROBOMECH Journal* 3, 8. doi:10.1186/s40648-016-0047-1.
- Kuo, A., 2007. Choosing Your Steps Carefully. *IEEE Robotics & Automation Magazine* 14, 18–29. doi:10.1109/MRA.2007.380653.
- Li, M., Guo, S., Hirata, H., Ishihara, H., 2017. A roller-skating/walking mode-based amphibious robot. *Robotics and Computer-Integrated Manufacturing* 44, 17–29. doi:10.1016/j.rcim.2016.06.005.

- Lin, Z., Zheng, W., Zhang, J., Ou, W., Yang, C., Huang, H., Xu, W., Yang, Z., Zhou, W., Zhang, Y., 2023. Mudskipper-inspired amphibious robotic fish enhances locomotion performance by pectoral-caudal fins coordination. *Cell Reports Physical Science* 4. doi:10.1016/j.xcrp.2023.101589.
- Liu, H., Curet, O., 2018. Swimming performance of a bio-inspired robotic vessel with undulating fin propulsion. *Bioinspiration & Biomimetics* 13, 056006. doi:10.1088/1748-3190/aacd26.
- Mignano, A.P., Kadapa, S., Tangorra, J.L., Lauder, G.V., 2019. Passing the Wake: Using Multiple Fins to Shape Forces for Swimming. *Biomimetics* 4, 23. doi:10.3390/biomimetics4010023.
- Milana, E., Raemdonck, B.V., Cornelis, K., Dehaerne, E., Clerck, J.D., Groof, Y.D., Vil, T.D., Gorissen, B., Reynaerts, D., 2020. EELWORM: a bioinspired multimodal amphibious soft robot, in: 2020 3rd IEEE International Conference on Soft Robotics (RoboSoft), pp. 766–771. doi:10.1109/RoboSoft48309.2020.9115989.
- Nygaard, T.F., Martin, C.P., Torresen, J., Glette, K., Howard, D., 2021. Real-world embodied AI through a morphologically adaptive quadruped robot. *Nature Machine Intelligence* 3, 410–419. doi:10.1038/s42256-021-00320-3.
- Ohashi, T., Yamada, H., Hirose, S., 2010. Loop forming snake-like robot ACM-R7 and its Serpenoid Oval control, in: 2010 IEEE/RSJ International Conference on Intelligent Robots and Systems, pp. 413–418. doi:10.1109/IROS.2010.5651467.
- Paifelman, E., Riccardi, G., Ciappi, E., 2024. Fluid-structure coupled analytical model for oscillatory fish-like propulsion. *Ocean Engineering* 299, 117292. doi:10.1016/j.oceaneng.2024.117292.
- Piskur, P., 2022a. Side Fins Performance in Biomimetic Unmanned Underwater Vehicle. *Energies* 15, 5783. doi:10.3390/en15165783.
- Piskur, P., 2022b. Strouhal Number Measurement for Novel Biomimetic Folding Fins Using an Image Processing Method. *Journal of Marine Science and Engineering* 10, 484. doi:10.3390/jmse10040484.

- Qiu, H., Chen, L., Ma, X., Bi, S., Wang, B., Li, T., 2023. Analysis of Heading Stability due to Interactions between Pectoral and Caudal Fins in Robotic Boxfish Locomotion. *Journal of Bionic Engineering* 20, 390–405. doi:10.1007/s42235-022-00271-4.
- Rafeeq, M., Toha, S.F., Ahmad, S., Razib, M.A., 2021. Locomotion Strategies for Amphibious Robots-A Review. *IEEE Access* 9, 26323–26342. doi:10.1109/ACCESS.2021.3057406.
- Ren, K., Yu, J., 2021. Research status of bionic amphibious robots: A review. *Ocean Engineering* 227, 108862. doi:10.1016/j.oceaneng.2021.108862.
- Shah, D., Yang, B., Kriegman, S., Levin, M., Bongard, J., Kramer-Bottiglio, R., 2021. Shape Changing Robots: Bioinspiration, Simulation, and Physical Realization. *Advanced Materials* 33, 2002882. doi:10.1002/adma.202002882.
- Shim, H., Yoo, S.y., Kang, H., Jun, B.H., 2016. Development of arm and leg for seabed walking robot CRABSTER200. *Ocean Engineering* 116, 55–67. doi:10.1016/j.oceaneng.2016.02.028.
- Sir James, L., 1975. *Mathematical biofluidynamics*. SIAM.
- Tong, B., Zhuang, L., Cheng, J., 1991. Hydrodynamic study of fish wave-swing propulsion. *Mechanics and Practice* 13, 17–26. [in Chinese].
- Wang, G., Chen, X., Yang, S., Jia, P., Yan, X., Xie, J., 2017. Subsea crab bounding gait of leg-paddle hybrid driven shoal crablike robot. *Mechatronics* 48, 1–11. doi:10.1016/j.mechatronics.2017.10.002.
- Wang, Z., Lou, J., Yang, H., Chen, T., Wei, Y., Xu, C., Cui, Y., 2023. Underwater dynamic hysteresis modeling and feedforward control of flexible caudal fin actuated by macro fiber composites. *Journal of Sound and Vibration* 556, 117717. doi:10.1016/j.jsv.2023.117717.
- White, C.H., Lauder, G.V., Bart-Smith, H., 2021. Tunabot Flex: a tuna-inspired robot with body flexibility improves high-performance swimming. *Bioinspiration & Biomimetics* 16, 026019. doi:10.1088/1748-3190/abb86d.

- Wu, M., Xu, X., Zhao, Q., Afridi, W.H., Hou, N., Afridi, R.H., Zheng, X., Wang, C., Xie, G., 2022. A Fully 3D-Printed Tortoise-Inspired Soft Robot with Terrains-Adaptive and Amphibious Landing Capabilities. *Advanced Materials Technologies* 7, 2200536. doi:10.1002/admt.202200536.
- Xia, M., Wang, H., Yin, Q., Shang, J., Luo, Z., Zhu, Q., 2023. Design and Mechanics of a Composite Wave-driven Soft Robotic Fin for Biomimetic Amphibious Robot. *Journal of Bionic Engineering* 20, 934–952. doi:10.1007/s42235-022-00328-4.
- Xing, H., Guo, S., Shi, L., He, Y., Su, S., Chen, Z., Hou, X., 2018. Hybrid Locomotion Evaluation for a Novel Amphibious Spherical Robot. *Applied Sciences* 8, 156. doi:10.3390/app8020156.
- Yang, Y., Xie, Y., Liu, J., Li, Y., Chen, F., 2024. 3D-Printed Origami Actuators for a Multianimal-Inspired Soft Robot with Amphibious Locomotion and Tongue Hunting. *Soft Robotics* doi:10.1089/soro.2023.0079.
- Yi, Y., Geng, Z., Jianqing, Z., Siyuan, C., Mengyin, F., 2015. Design, modeling and control of a novel amphibious robot with dual-swing-legs propulsion mechanism, in: 2015 IEEE/RSJ International Conference on Intelligent Robots and Systems (IROS), pp. 559–566. doi:10.1109/IROS.2015.7353427.
- Yin, Q., Shang, J., Jiang, T., Bai, X., Wang, H., Luo, Z., 2021. Fin surface structure design and motion simulation of flexible undulating fin amphibious robot. *Journal of Engineering Thermophysics* 42, 2954–2959. [in Chinese].
- Yu, J., Ding, R., Yang, Q., Tan, M., Wang, W., Zhang, J., 2012. On a Bio-inspired Amphibious Robot Capable of Multimodal Motion. *IEEE/ASME Transactions on Mechatronics* 17, 847–856. doi:10.1109/TMECH.2011.2132732.
- Yue, C., Guo, S., Li, M., 2013. ANSYS FLUENT-based modeling and hydrodynamic analysis for a spherical underwater robot, in: 2013 IEEE International Conference on Mechatronics and Automation, pp. 1577–1581. doi:10.1109/ICMA.2013.6618149.

- Zhang, S., Zhou, Y., Xu, M., Liang, X., Liu, J., Yang, J., 2016. AmphiHex-I: Locomotory Performance in Amphibious Environments With Specially Designed Transformable Flipper Legs. *IEEE/ASME Transactions on Mechatronics* 21, 1720–1731. doi:10.1109/TMECH.2015.2490074.
- Zhong, B., Zhang, S., Xu, M., Zhou, Y., Fang, T., Li, W., 2018. On a CPG-Based Hexapod Robot: AmphiHex-II With Variable Stiffness Legs. *IEEE/ASME Transactions on Mechatronics* 23, 542–551. doi:10.1109/TMECH.2018.2800776.